ACS OMEGA

http://pubs.acs.org/journal/acsodf

Article

Multifunctional Ternary NLP/ZnO@L-cysteine-*grafted*-PANI Bionanocomposites for the Selective Removal of Anionic and Cationic Dyes from Synthetic and Real Water Samples

Ritu Bir,[§] Mohd Saquib Tanweer,*[,§] Meenakshi Singh, and Masood Alam*

Cite This: *ACS Omega* 2022, 7, 44836−44850

Read Online

ACCESS | Metrics & More | Article Recommendations | Supporting Information

ABSTRACT: The development of competent adsorbents based on agro-waste materials with multifunctional groups and porosity for the removal of toxic dyes from aqueous solutions is still a challenge. Herein, a bionanocomposite made up of neem leaf powder (NLP), zinc oxide (ZnO), and amino acid (L-cysteine)-functionalized polyaniline (PANI), namely, NLP/ZnO@L-cysteine-*grafted*-PANI (NZC-*g*-PANI), has been prepared by an in situ polymerization method. The as-prepared bionanocomposite was tested for the adsorptive removal of three anionic dyes, namely, methyl orange (MO), amido black 10B (AB 10B), and eriochrome black T (EBT), as well as three cationic dyes, namely, brilliant green (BG), crystal violet (CV), and methylene blue (MB), from synthetic aqueous medium. The morphological and structural characteristics of the NZC-*g*-PANI nanocomposite were examined with the help of HR field emission scanning electron microscopy (FESEM), transmission electron microscopy (TEM), X-ray diffraction (XRD), Fourier transform infrared (FTIR), and Raman spectroscopy. FTIR and Raman studies show that the formulated NZC-*g*-PANI have an ample number of functional moieties such as carboxyl (−COOH), hydroxyl (−OH), amines ($-NH_2$), and imines (−N═), thus demonstrating outstanding dye removal capacity. C−S linkage helps to attach L-cysteine with polyaniline. Moreover, the predominance of chemisorption via ionic/pi−pi interaction and hydrogen bonding between the NZC-*g*-PANI nanocomposite and dyes (BG and MO) has been realized by FTIR and fitting of kinetics data to the PSO model. For both BG and MO dyes, the biosorption isotherm was precisely accounted for by the Langmuir isotherm with q_{max} values of up to 218.27 mg g^{-1} for BG at pH 6 and 558.34 mg g^{-1} for MO at pH 1. Additionally, thermodynamic studies revealed the endothermic and spontaneous nature of adsorption. NZC-*g*-PANI showed six successive regeneration cycles for cationic (MO: from 96.3 to 90.4%) and anionic (BG: from 94.7 to 88.7%) dyes. Also, batch adsorption operations were validated to demonstrate dye biosorption from real wastewater, such as tap water, river water, and laundry wastewater. Overall, this study indicates that the prepared NZC-*g*-PANI biosorbent could be used as an effective adsorbent for the removal of various types of anionic as well as cationic dyes from different aqueous solutions.

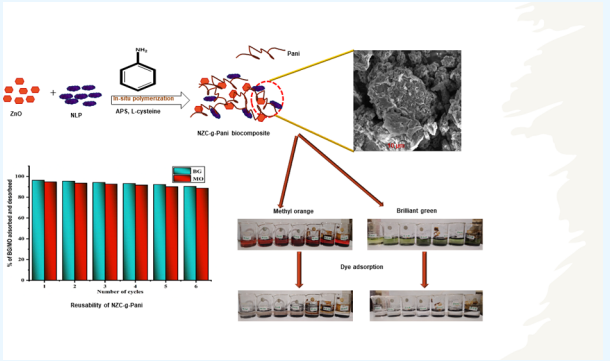

1. INTRODUCTION

The exponential growth of the population has led to rapid industrialization, which has played a crucial role in the proliferation of water pollution. Wastewater discharged from dye, food, textile, and paper industries is a major source of effluents into water bodies. Dyes, though used in small amounts, are highly observable. Around the world, nearly 700,000 tonnes of organic dyes are used in the textile industry.[1] When these effluents are released into water, they contain a high concentration of synthetic and organic dyes that are toxic to aquatic and human life at even very low concentrations. It causes skin rashes, dysfunction of organs like the liver and kidney, neurological issues, and potential mutagenic and carcinogenic effects.[2−4] Most of the dyes released into water as effluents are nonbiodegradable and quite stable. Dyes also affect the photosynthetic capability of aquatic plants by limiting sunlight penetration in the water body.[5] At low concentrations, dyes even decrease dissolved oxygen content, and gas solubility therefore increases BOD, COD, TOC, and TDS levels.[6] Dyes are mainly made up of dye agents and dye enhancers. Water is colored by the dye agent, which is amplified by the dye enhancer to make the dye soluble in water and adhere to surfaces. Thus, the dyes that infiltrate into water supply untreated endanger ecotoxicological damage.[7] In the coming years, as the population continues to grow

Received: August 3, 2022
Accepted: November 15, 2022
Published: November 30, 2022

exponentially, there will be greater stress on meeting the demand for clean water. The ill effects of dyes on mankind and the environment have forced scientists and researchers around the world to focus their attention on dye removal from aqueous solutions.

In the past few decades, several processes like coagulation,[8] ion exchange,[9] reverse osmosis,[10] membrane separation process,[11] flocculation,[12] and photocatalysis[13−15] methods have been used for water purification, but each method has its own limitations. However, these water filtration techniques are expensive, produce secondary contaminants, need additional processing, use a lot of energy, and have low sequestration of the targeted contaminants over time. Among the above methods, biosorption is gaining popularity as an efficient method for the treatment of wastewater due to its high efficiency and low-cost regeneration, recovery of adsorbates, no sludge formation, and availability of different materials that can be used as adsorbents.[3,4,16−19]

Unmodified agricultural waste materials such as vegetable peels, fruit peels, sago waste, rice husks, and other plant waste have been directly employed as biosorbents for water purification. But unmodified agricultural waste materials show less adsorption capacity toward water pollutants. So, biosorbents need to be changed chemically to improve their maximum adsorption potential by increasing their specific surface area, the number of active sites, and the number of functional groups. The seeds and leaves of the neem tree (*Azadirachta indica*) have enormous medicinal values and have been used since ancient times to cure human ailments in the Indian subcontinent.[20] Unfortunately, neem seeds and leaves become waste after shedding during the summer months in India. Therefore, a simple idea has been exploited to chemically modify these leaves (in the form of powder) to obtain a bionanocomposite with enhanced adsorption capacity compared with bare neem leaf powder. This approach may reduce the plant-waste materials from the environment and may also be efficiently used to sequestrate water pollutants.

Several methods including lithography, laser ablation, aerosol techniques, radiolysis, and photochemical reduction can be used for various nanoparticle synthesis. These techniques are typically expensive, energy-intensive, or dangerous for humans and the environment.[21] For instance, in the chemical synthesis of nanoparticles, dispersants, surfactants, or chelating agents are used to prevent accumulation and control the growth of particles. The majority of these reagents can be regarded as environmental contaminants when they are utilized in large quantities.[22] Thus, emphasis is being paid nowadays to the synthesis of nanoparticles that are environmentally friendly and use biologically prepared nanoparticles, which involve the use of various parts of plants or their products as biosorbents.[23] Among various nanoparticles, zinc oxide nanoparticles (ZnO NPs) are a class of multifunctional inorganic nanoparticles considered ideal for having many distinct features. In addition, chemically synthesized ZnO NPs do not show toxic effects on humans when exposed in small concentrations, although high doses can show lethal effects.[24]

Polyaniline (PANI), which is a conducting polymer, has been used in a variety of applications, including electrodes of lightweight batteries, energy storage, sensors, electromagnetic shielding devices, and anticorrosion coatings.[25−27] Literature studies show that PANI is a good choice as an adsorbent for removing dyes like methyl orange, brilliant green, Congo red, amido black 10B, malachite green, and eosin yellow from water solutions because it is easy to make, stable and easy to dope and has good conducting surfaces.[3,28]

Researchers are focusing on the use of nanoparticles for the treatment of water due to their efficiency in adsorption and potent catalytic activity. But due to the small size of nanoparticles, there is a problem in the recovery of nanoparticles from treated water. Due to the easy recovery of composite adsorbents, nanoparticle impregnation on a support to form a composite adsorbent is also gaining popularity. These composite adsorbents show better efficiency due to the presence of various active sites for adsorbate uptake.[7]

The novelty of this research is as follows: (a) the NLP/ZnO@L-cysteine-*grafted*-PANI (NZC-*g*-PANI) nanocomposite has a unique rough and porous surface, which has a high adsorption capacity due to the availability of multifunctional groups for the adsorption compared to other conventional adsorbents; (b) the NZC-*g*-PANI nanocomposite is based on agro-waste materials, ultimately making it an efficient, cost-effective, recyclable, and eco-friendly adsorbent; (c) the NZC-*g*-PANI nanocomposite is employed to sequestrate dyes from synthetic as well as real wastewater samples. Also, the biosorption of methyl orange (MO) and brilliant green (BG) dyes by the NZC-*g*-PANI nanocomposite has been looked at in terms of isotherms, kinetics, and thermodynamics.

2. EXPERIMENTAL SECTION

2.1. Materials. Aniline monomer [$C_6H_5NH_2$], ammonium persulfate (APS) [$(NH_4)_2S_2O_8$], hydrochloric acid [HCl], zinc acetate dihydrate [$ZnC_4H_6O_4$], poly(ethylene glycol) (PEG; as a surfactant), monoethanolamine [C_2H_7NO], L-cysteine [$C_3H_7NO_2S$], methanol [CH_3OH], ethanol [C_2H_5OH], acetone [C_3H_6O], sodium hydroxide [NaOH], potassium nitrate [KNO_3], three anionic dyes, namely, methyl orange [$C_{14}H_{14}N_3NaO_3S$], amido black 10B [$C_{22}H_{14}N_6Na_2O_9S_2$], eriochrome black T [$C_{20}H_{12}N_3O_7SNa$], and three cationic dyes, namely, brilliant green [$C_{27}H_{34}N_2O_4S$], crystal violet [$C_{25}N_3H_{30}Cl$], and methylene blue [$C_{16}H_{18}ClN_3S$], were purchased from Merck Pvt., Ltd. The structures and some features of the selected dyes are provided in Figure S1 and Table S1, respectively. Double-distilled water (DDW) was used in all experimental processes.

2.2. Preparation of Neem Leaf Powder (NLP). Fresh neem leaves were collected from the garden of Jamia Millia Islamia, New Delhi, India. These were washed several times with tap water to remove dust and other soluble impurities. These were allowed to dry first at room temperature, followed by air-drying in an oven at 27 ± 3 °C for 2 days till the leaves became crisp. Then, the dried leaves were mechanically crushed into a fine powder by a mechanical grinder to procure the neem leaf powder (NLP). The NLP was sieved by a sieve tray (BSS 72/ASTM70), and a 212 μm fraction was separated, followed by further washing with DDW till the washings became clear. Finally, washed NLP was air-dried for 24 h in an oven at 27 ± 3 °C and stored in a precleaned glass. It was kept in a desiccator to avoid environmental moisture.

2.3. Preparation of ZnO Nanoparticles. ZnO nanoparticles were prepared as reported in ref 29. First, 2 g of zinc acetate was dissolved in 70 mL of DDW with a magnetic stirrer (1000 rpm) for an hour to obtain a clear solution. Polyethylene glycol (0.1% (w/v)), which acted as a surfactant, and 10 mL of monoethanolamine were slowly added to the solution and stirred for another 30 min until the solution became clear. The

https://doi.org/10.1021/acsomega.2c04936
ACS Omega 2022, 7, 44836−44850

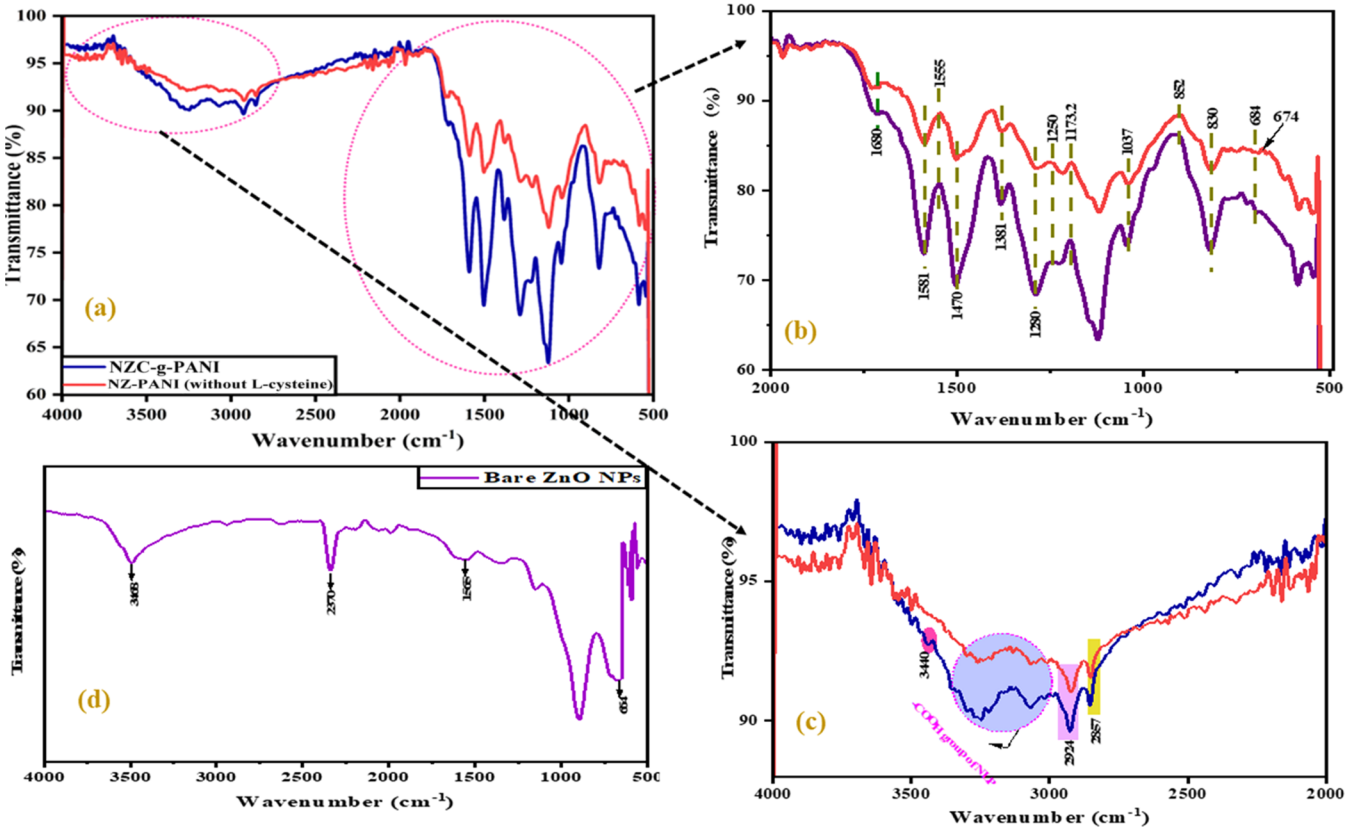

Figure 1. FTIR in the range of 4000−500 cm^{-1} (a). Zoom in the ranges of 2000−500 cm^{-1} (b) and 4000−2000 cm^{-1} (c). Spectra of NZ-PANI (without L-cysteine functionalization) and NZC-*g*-PANI nanocomposites and bare ZnO NPs (d).

content was then transferred to a Teflon-capped autoclave for 3 h at 140 °C. The resultant was washed with DDW and ethanol by centrifugation (8000 rpm). It was then dried at 80 °C in a hot air oven for 12 h, followed by calcination in a muffle furnace for 2 h at 400 °C.

2.4. Preparation of NZC-*g*-PANI Nanocomposites. ZnO and NLP with a weight ratio of 1:2 (w/w) were dispersed in 100 mL of 1 M HCl in a 250 mL beaker and were magnetically stirred at 1000 rpm for 30 min. Then, 0.6 g of L-cysteine was added ultrasonically for 1 h to it, and 1 mL of aniline monomer was also added to the above mixture. After that, 50 mL of 1 M HCl and 0.023 mol of ammonium persulfate (APS) were added dropwise and then stirred for another 12 h. The resultant was obtained after washing with DDW, methanol, and acetone several times. Then, the filtered material was put in an air oven and dried at 80 °C for one night to make a ternary biocomposite or NZC-*g*-PANI. It was used as a biosorbent for the removal of various cationic as well as anionic dyes.

2.5. Characterization of NZC-*g*-PANI Nanocomposites. The Fourier transform infrared (FTIR) spectra of bare NLP, bare ZnO NPs, and the NZC-*g*-PANI nanocomposite (before and after MO and BG dye adsorption) were investigated in the range of 4000−400 cm^{-1} using a Perkin Elmer (Nicolet 6700, Thermo Fisher). High-resolution field emission scanning electron microscopy (HR FESEM) was used to record the microstructure of the NZC-*g*-PANI nanocomposite (before and after dye adsorption) employing a Zeiss NOVA NANOSEM-450 field emission scanning electron microscope. The NZC-*g*-PANI nanocomposite was also analyzed using a transmission electron microscope (JEM 2100, JEOL, Japan) instrument operating at 200 kV. Raman spectra of the samples were carried out at room temperature by an inVia Reflex Raman Microscope (Renishaw, United Kingdom) with the samples deposited on the glass slides. X-ray diffraction (XRD) measurements were performed on a Rigaku D/max-RA X-ray diffractometer. The diffracted intensity of the Cu Kα radiation (λ = 0.154 nm, 45 kV, 40 mA) was evaluated in the 5−80° 2θ range. The dye concentrations in the treated samples were determined using a spectrophotometer (Shimadzu UV-2450, Japan). The pH at the point of zero charge (pH_{pzc}) was determined using a change in pH approach with a pH meter (ANALAB Scientific pH/ORP Analyzer).

2.6. Batch Adsorption Experiments. A stock solution containing 1000 mg L^{-1} of all selected dyes such as MO, AB 10B, EBT, BG, CV, and MB was prepared by dissolving 1 g of each dye (analytical grade) in 1000 mL of DDW. All of the batch experimental solutions for biosorption of dye studies were prepared by appropriate dilutions from the stock solution. Batch adsorption experiments were carried out with 0.025 g of the NZC-*g*-PANI adsorbent dose with 30 mL of 50 mg L^{-1} of each dye and shaking on a rotary shaker (250 rpm) for one day at 25 ± 3 °C. The residual concentration of dyes in treated water samples was determined by measuring the absorbance of MO, AB 10B, EBT, BG, CV, and MB at 464, 630, 489.95, 625, 590, and 665 nm, respectively. The yield of removal efficiency (%*R*) and dye performance uptake (q_e; mg g^{-1}) were calculated using Formulas 1 and 2, respectively.[30,31]

$$\%R = \frac{C_o - C_e}{C_e} \times 100 \quad (1)$$

https://doi.org/10.1021/acsomega.2c04936
ACS Omega 2022, 7, 44836−44850

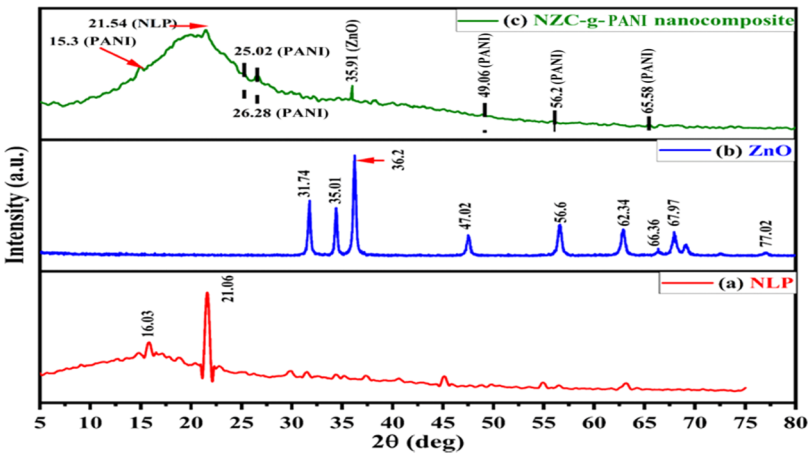

Figure 2. X-ray diffraction patterns of NLP (a), ZnO NPs (b), and NZC-*g*-PANI (c).

$$q_e = \frac{(C_o - C_e)}{m} V \quad (2)$$

where C_o and C_e are the concentrations before adsorption and after adsorption (mg L^{-1}), respectively. m (g) is the amount of the NZC-*g*-PANI nanocomposite, and V (L) is the volume of the dye solution.

2.7. Dye Selectivity Study. The NZC-*g*-PANI nanocomposite was evaluated using MO, AB 10B, EBT, BG, CV, and MB as adsorbates for selectivity tests at neutral pH and room temperature (25 ± 3 °C). The dye removal efficiency was observed as MO (100%) > BG (99.7%) > AB 10B (74.2%) > CV (70.81%) > EBT (65.6%) > MB (65.38%) and is presented in Figure S2. On the basis of dye removal efficiency, only two dyes, i.e., BG and MO, were selected for further adsorption analysis.

2.8. Comparative Study of Pristine PANI, Pristine ZnO, Pristine NLP, and NZC-*g*-PANI Adsorbent for MO and BG Dye Removal. The dye removal efficiency of pristine ZnO, pristine PANI, pristine NLP, and NZC-*g*-PANI was investigated at neutral pH. For this, an adsorbent dose of 0.025 g, MO and BG concentration of 50 mg L^{-1}, was separately added to the respective Erlenmeyer flask and shaken in a rotary shaker (250 rpm) for 24 h at 25 ± 3 °C. After equilibrium attainment, the %R of individual adsorbent materials was calculated using eq 1. The trend of the %R of all of the adsorbent material for both MO and BG dyes (Figure S3) was reported as follows: NZC-*g*-PANI > PANI > ZnO > NLP.

2.9. Recyclability Test. To investigate the stability and reusability of NZC-*g*-PANI, the simultaneous BG and MO dye adsorption−desorption tests were executed for up to six cycles. The adsorption experiments for both dyes were performed with 50 mg L^{-1} BG/MO dye, NZC-*g*-PANI dose of 0.3 g, and at preoptimized solution pH, shaken at 250 rpm. After the attainment of equilibrium, NZC-*g*-PANI was filtered from the solution using a centrifugation machine. In desorption experiments, BG and MO dye-loaded NZC-*g*-PANI was added to 30 mL of 0.1 M NaOH and shaken. After the desorption, NZC-*g*-PANI was washed with a 0.1 N HCl solution followed by drying for reuse in the adsorption experiment.

2.10. Point of Zero Charge. The solid addition method[32] was used to measure the zero point charge of the NZC-*g*-PANI nanocomposite using a 0.01 M KNO_3 solution. First, 50 mL of KNO_3 solution was transferred to 10 Erlenmeyer flasks of 100 mL capacity. To each flask, 0.15 g of the NZC-*g*-PANI nanocomposite adsorbent was added. The pH of the solution was adjusted between 1 and 10 by the addition of either 0.1 N HCl or 0.1 N NaOH, and the flasks were covered and shaken intermittently for 24 h. The resultant pH was noted, and the difference between the initial and final pH values was calculated. The initial pH was plotted against ΔpH, and the intersection point of the obtained curve was taken as pH_{pzc}.

3. RESULTS AND DISCUSSION

3.1. Characterization. *3.1.1. Fourier Transform Infrared Spectroscopy.* Figure 1 shows the FTIR spectra of ZnO NPs and NZ-PANI (without L-cysteine functionalization) and NZC-*g*-PANI nanocomposites. In Figure 1d, absorption peaks observed at wavenumbers of 3468 and 1565 cm^{-1} confirm the synthesis of pure ZnO NPs.[33] The band at 2370 cm^{-1} shows the H−O−H vibration of water molecules. The peak at 664 cm^{-1} corresponds to the ZnO hexagonal phase.[34] Due to out-of-plane CH bending vibrations, ZnO NPs and NZC-*g*-PANI and NZ-PANI (without L-cysteine functionalization) nanocomposites revealed a strong characteristic band at about 830 cm^{-1}, which indicates that para coupling, i.e., polymerization, happens at the 1−4 position.[35] It validates the adhesion of ZnO NPs to the polymer matrix. In addition, in Figure 1a,b,d, small peaks are observed in the region between 650 and 500 cm^{-1}, which are assigned to the metal−oxygen vibration (Zn−O) of ZnO NPs.[36] In Figure 1c, the peak of the NZC-*g*-PANI bionanocomposite at 3440 cm^{-1} is associated with O−H stretching and confirms the presence of L-cysteine.[37] The short band at 674 cm^{-1} represents the C−S linkage of the cysteine group to the PANI of NZC-*g*-PANI (Figure 1b),[38] while this band is found absent in the case of the unmodified nanocomposite, i.e., NZ-PANI (without L-cysteine). The various bands of PANI shown in Figure 1b, which appeared at 852, 1173.2, 1280, 1381, and 1680 cm^{-1}, are attributed to NH and CH stretching vibrations, benzenoid ring, and NH_2 bending modes.[39,40] In addition to the above peaks, the spectrum of PANI exhibits peaks at 684 and 1581 cm^{-1}, which may be related to NH_2 wagging and the presence of an imine functional group.[39] The peaks at 1555 and 1470 cm^{-1} may be attributed to the stretching bands of nitrogen quinoid (N═Q═N) and benzenoid (N−B−N) units, which makes PANI a conducting nature polymer.[41]

The FTIR spectra of NLP are also found in NZ-PANI (without L-cysteine functionalization) and NZC-*g*-PANI nano-

https://doi.org/10.1021/acsomega.2c04936
ACS Omega 2022, 7, 44836−44850

composites, as shown in Figure 1c. The bands at 1037 and 1250 cm^{-1} can be attributed to O−H stretching, while bands at 2857 and 2924 cm^{-1} are due to the C−H stretching of methylene groups on the NLP surface and chelated H bridges, respectively.[42] Figure 1c shows the broad band from 3370 to 3154 cm^{-1}, representing the O−H stretching vibration mode in the carboxylic acid groups of NLP.[43]

3.1.2. High-Resolution X-ray Diffraction. XRD analysis of ZnO NPs (Figure 2b) shows high and sharp peaks with 2θ values at 31.74, 35.01, 36.2, 47.02, 56.6, 62.34, 66.36, 67.97, and 77.02° which confirm the wurtzite (hexagonal) structure of ZnO NPs.[44] The peaks of ZnO NPs seen in the XRD pattern perfectly match JCPDS card no. 36-1451.[45] It is therefore reasonable to record that ZnO NPs have been successfully synthesized. Figure 2a shows the XRD pattern of NLP in which weak peaks at 16.03 and 21.026° are attributed to the presence of cellulose in NLP. The XRD pattern of NLP is characteristically amorphous in nature due to the presence of hemicellulose and lignin in the biomass.[30] The sharp diffraction peaks at 2θ values of 31.74, 35.01, 36.2, 47.02, and 56.6° correspond to planes of ZnO NPs, which further assures that ZnO is successfully embedded in the matrix of PANI.[35]

Further, the XRD pattern of the NZC-*g*-PANI nanocomposite (Figure 2c) confirms that ZnO NPs and NLP were successfully incorporated into the PANI matrix, as is also evident from the FTIR spectra. The characteristic peaks of PANI in an amorphous state show weak reflections at 2θ values of 49.06, 56.2, and 65.58°, thereby confirming the report of Anand et al.[35] Peaks of 2θ values at 15.3, 25.02, and 26.28° are the characteristic peaks of PANI.[46] Overall, the as-prepared bionanocomposite, i.e., NZC-*g*-PANI, seems to be amorphous in nature.

3.1.3. High-Resolution Raman Spectroscopy. All of the materials were also characterized by Raman spectroscopy. The Raman spectra of bare ZnO NPs and the NZC-*g*-PANI nanocomposite are shown in Figure 3. It was observed that the

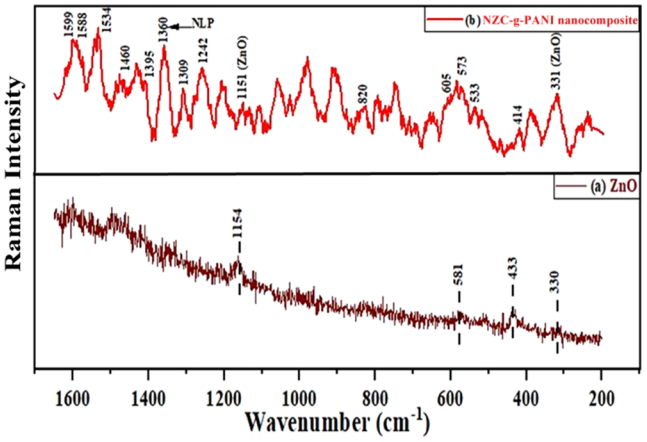

Figure 3. Raman spectra of bare ZnO NPs (a) and NZC-*g*-PANI nanocomposite (b).

Raman spectrum of ZnO NPs (Figure 3a) is in a regular Raman manner, and the characteristic peaks are observed at 1154, 581, 437, and 330 cm^{-1}, confirming the wurtzite structure of ZnO.[1,47] Figure S4 represents the Raman spectra of NLP. Plant-based materials contain lignin and cellulose. Several bands between 1500 and 1660 cm^{-1} are due to lignin in the NLP. As shown in Figure S4 (zoomed part), prominent bands at 1576, 1607, and 1628 cm^{-1} are because of stretching vibrations of the aryl ring of coniferyl aldehyde and coniferyl alcohol of lignin.[48] On the other hand, bands at 1461, 1376, and 1092 cm^{-1} are due to the deformation vibration of aldehydes and C−C and C−O stretching modes of aldehydes of cellulose. Additionally, several bands are seen in Figure S4 (zoomed part) between 1200 and 850 cm^{-1}, confirming the cellulose of NLP.

In Figure 3b, the nanocomposite shows bands at 1239 and 1168 cm^{-1}, which are assigned to C−H bending vibrations of benzenoid-like aromatic rings and C−N stretching of the secondary aromatic amine of PANI,[49,50] respectively. The absorption at 1174, 1498, and 1597 cm^{-1} is due to the benzenoid ring (C−H bending), C═N stretching in emeraldine base (imine), and quinoid ring (C═C stretching),[51,52] respectively. The peak at 1456 cm^{-1} associated with the C═N stretching mode of the quinoid units confirms the doped PANI structure. In addition, absorption at 572, 607, 417, 811, and 530 cm^{-1} may be associated with the doped PANI structure.[53,54] The Raman data coupled with FTIR provide clear evidence of a large number of imine and amine groups in the PANI nanocomposites. Furthermore, peaks at 1360 and 1588 cm^{-1} are associated with NLP,[55] while the peaks at 331 and 1151 cm^{-1} represent ZnO NPs[44,47] in PANI-based nanocomposites.

3.1.4. High-Resolution Field Emission Scanning Electron Microscopy. HR FESEM has been employed as a vital tool for the characterization of adsorbent materials. SEM can reveal the surface morphology of the adsorbent. It determines the shape, particle size, and pore size distribution of the adsorbent material. The surface morphology of the NZC-*g*-PANI nanocomposite when examined with the help of HR FESEM showed the presence of a rough and porous surface where targeted BG and MO dyes can be trapped and adsorbed. A number of heterogeneous pores can also be seen in Figure 4a. The pores in the NZC-*g*-PANI composite are due to the functionalization of amino acid, i.e., L-cysteine, which ultimately helps in the sequestration of targeted pollutants. The same study has been shown by Hsini et al.[56] After biosorption, significant changes can be easily observed in Figure 4b,c. Figure 4b,c shows that pores have been packed by dyes and the lining of pores has thickened, indicating the occurrence of biosorption.

3.1.5. Transmission Electron Microscope. TEM analysis was performed to gain insight into the morphology of the NZC-*g*-PANI bionanocomposite. The corresponding outcomes are displayed in Figure 4d. The morphological structure of NZC-*g*-PANI presents the flat layered structures of PANI and NLP, which are tightly stacked together, indicating successful modification. It is identified from Figure 4d that ZnO NPs are coated on PANI/NLP layers. We also observe that ZnO NPs onto PANI/NLP layers are dense, but their thickness and distribution seem to be nonuniform, as also seen in the SEM image. It is important to note that even though the TEM sample was sonicated for a long time, a large number of ZnO NPs stayed tightly attached to the PANI/NLP layer. This shows that ZnO NPs and PANI/NLP interact strongly.

3.2. Effect of pH. The pH of the solution is an important parameter in adsorption studies. The adsorption capacity of an adsorbent is influenced both by the surface of the sorbent and the degree of ionization of the functional groups present in the adsorbate. In our study, the pH effect on the NZC-*g*-PANI

https://doi.org/10.1021/acsomega.2c04936
ACS Omega 2022, 7, 44836−44850

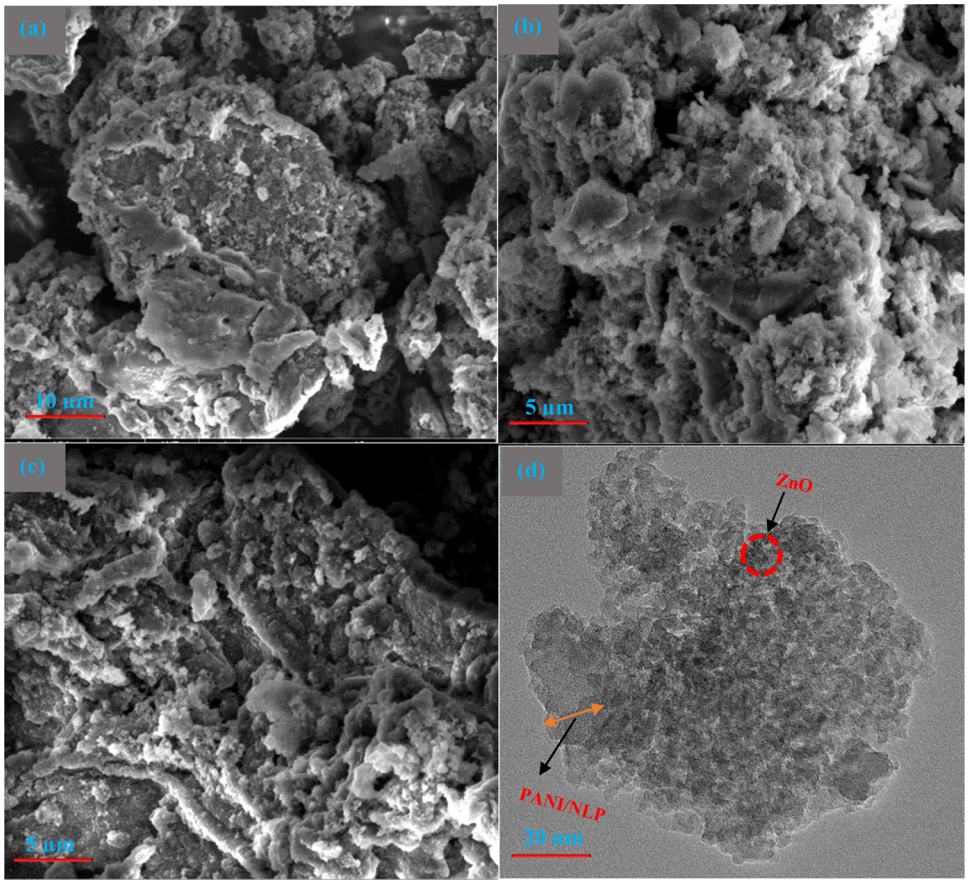

Figure 4. SEM of the NZC-*g*-PANI nanocomposite before (a) and after the adsorption of MO (b) and BG (c) dyes. Transmission electron microscopy (TEM) image of the NZC-*g*-PANI nanocomposite (d).

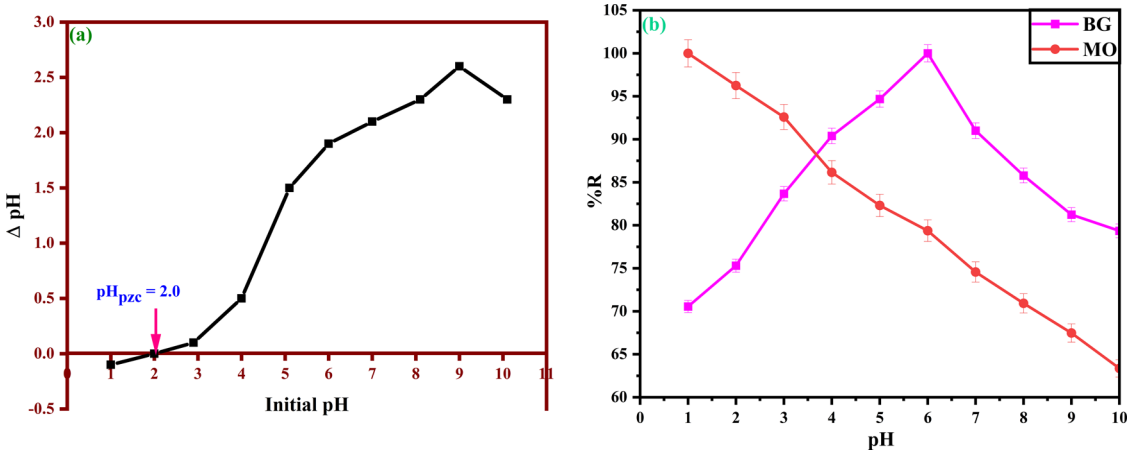

Figure 5. pH_{pzc} for the NZC-*g*-PANI nanocomposite (a), and the effect of pH on the adsorption of MO and BG (b) dyes.

nanocomposite was studied with the help of 50 mg L^{-1} BG and MO dyes. pH was varied from 1 to 10 by a 0.1 N HCl/NaOH solution to find out the most optimum pH for BG and MO dye adsorption, which can be seen in Figure 5b. The pH_{pzc} of the NZC-*g*-PANI nanocomposite is observed at about 2.0, as is clear from Figure 5a. At pH > pH_{pzc}, the NZC-*g*-PANI surface has a negative charge, while at pH < pH_{pzc}, NZC-*g*-PANI has a positive charge. The obtained results suggest that there is a decrease in the MO percentage removal with an increase in pH. A maximum percent removal of ∼100% of MO onto NZC-*g*-PANI takes place at a pH value of 1, while there is an increase in BG percentage removal with an increase in pH. At low pH values (pH < 2.0), the NZC-*g*-PANI nanocomposite with a positive surface charge facilitates stronger interactions with anionic contaminants, i.e., MO dye. In contrast, at high pH values (pH > 2.0), the NZC-*g*-PANI nanocomposite with a negative surface charge reveals a high affinity toward cationic BG dye.[57,58]

3.3. Effect of NZC-*g*-PANI Dose. The effect of NZC-*g*-PANI dose on the percentage removal of BG and MO dyes and the adsorption capacity of the biosorbent were studied. A varying amount of the NZC-*g*-PANI sorbent (0.01−0.07 g)

https://doi.org/10.1021/acsomega.2c04936
ACS Omega 2022, 7, 44836−44850

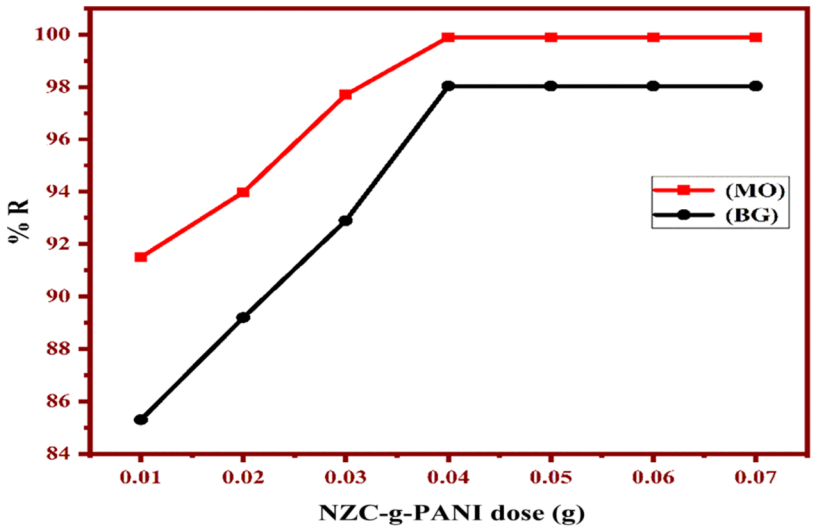

Figure 6. Effect of NZC-*g*-PANI dosages for the adsorption of MO and BG dyes.

Table 1. Variables of PFO and PSO Models for the Adsorption of MO and BG Dyes on the NZC-*g*-PANI

	PFO				PSO			
pollutant	q_e^{exp}(mg g^{-1})	q_e^{cal}(mg g^{-1})	K_1 (min^{-1})	R^2	q_e^{exp}(mg g^{-1})	q_e^{cal}(mg g^{-1})	K_2(g mg^{-1} min^{-1})	R^2
BG	49.77	13.70	−0.00132	0.572	49.77	50.25	0.0182	0.999
MO	49.87	3.966	−0.00038	0.828	49.87	50.15	0.0163	0.999

was added to 50 mg L^{-1} BG and MO dyes in a 100 mL Erlenmeyer flask. The flasks were covered and shaken for 2 h using a shaking incubator to attain equilibrium. Samples were centrifuged, and the supernatant was placed in a UV spectrophotometer to determine the residual concentration of the dye in the aqueous solution.

On increasing the NZC-*g*-PANI dose from 0.01 to 0.04 g, the adsorption capacity of NZC-*g*-PANI was enhanced toward cationic BG as well as anionic MO dye due to an increase in the number of pores present on the adsorbent and adsorption sites. Further increase in NZC-*g*-PANI dose resulted in no additional increase in BG and MO adsorption, as shown in Figure 6. At high dosages of the adsorbent, dye molecules are comparatively fewer in numbers to combine with all of the adsorption sites present on the NZC-*g*-PANI adsorbent, which gets exhausted, resulting in the reduction of adsorbent per unit mass adsorption capacity.[37] Adsorption tends to reach an equilibrium when the adsorption mass reaches a particular value. Equilibrium was reached after 0.04 g of adsorbent dose for both BG and MO dyes.

3.4. Contact Time and Adsorption Kinetics. The contact time study is essential for designing batch experiments. The adsorption capacity of MO and BG dyes on the NZC-*g*-PANI nanocomposite steadily increases with the increase in contact time (Figure S5a). A constant adsorption capacity was achieved after 60 min for both MO and BG dyes. Comparative adsorption of MO and BG dyes onto the NZC-*g*-PANI adsorbent shows that the MO (q_t = 119.61 mg g^{-1}) dye was sequestrated slightly more than the BG (q_t = 119.44 mg g^{-1}) dye, and the adsorption rate gradually decreased for both MO and BG, thus reaching an equilibrium. During the initial phases of adsorption, many vacant sites are available on the NZC-*g*-PANI nanocomposite, which, with the passage of time, decreases. Left out, vacant sites of NZC-*g*-PANI become difficult to occupy by BG and MO dyes due to existing repulsive forces between solute particles found on the solid adsorbent and adsorbate molecules, resulting in the slowing of the adsorption rate eventually.[59]

Adsorption kinetics is responsible for controlling the adsorption rate, which also determines the time needed for the adsorption process to reach equilibrium. Adsorption kinetics also gives information about the path used for adsorption and the mechanism involved in the adsorption process. To investigate the adsorption of BG and MO on the NZC-*g*-PANI nanocomposite, pseudo-first-order (PFO) and pseudo-second-order (PSO) kinetic models were used.

3.4.1. Pseudo-First-Order Kinetics. The pseudo-first-order kinetic model is the earliest known equation that describes the rate of adsorption based on adsorption capacity. It involves the reactions between functional groups that are present on adsorbent and adsorbate atoms, ions, or molecules by the formation of cation exchange reactions. The linear form of the pseudo-first-order equation[59] is as follows

$$\log(q_e - q_t) = -\frac{k_1 t}{2.303} + \log q_e \quad (3)$$

where q_e (mg g^{-1}) is the amount of the dye adsorbed by the adsorbent at equilibrium. q_t (mg g^{-1}) is the amount of the BG/MO dye adsorbed by NZC-*g*-PANI at varying times in min. K_1 is the rate constant of pseudo-first-order kinetics.

A graph of straight-line $\log(q_e - q_t)$ vs time was plotted, as shown in Figure S5b. The correlation coefficient (R^2) of BG is 0.572 and that of MO is 0.828 (Table 1), which shows that the adsorption of both dyes does not follow the PFO model.

3.4.2. Pseudo-Second-Order Kinetics. Ho and Mckay[60] gave the pseudo-second-order kinetic model for the adsorption of adsorbates and made the following assumptions:

(a) Adsorption occurs in localized areas, and no interaction is seen between adsorbed molecules.

https://doi.org/10.1021/acsomega.2c04936
ACS Omega 2022, 7, 44836−44850

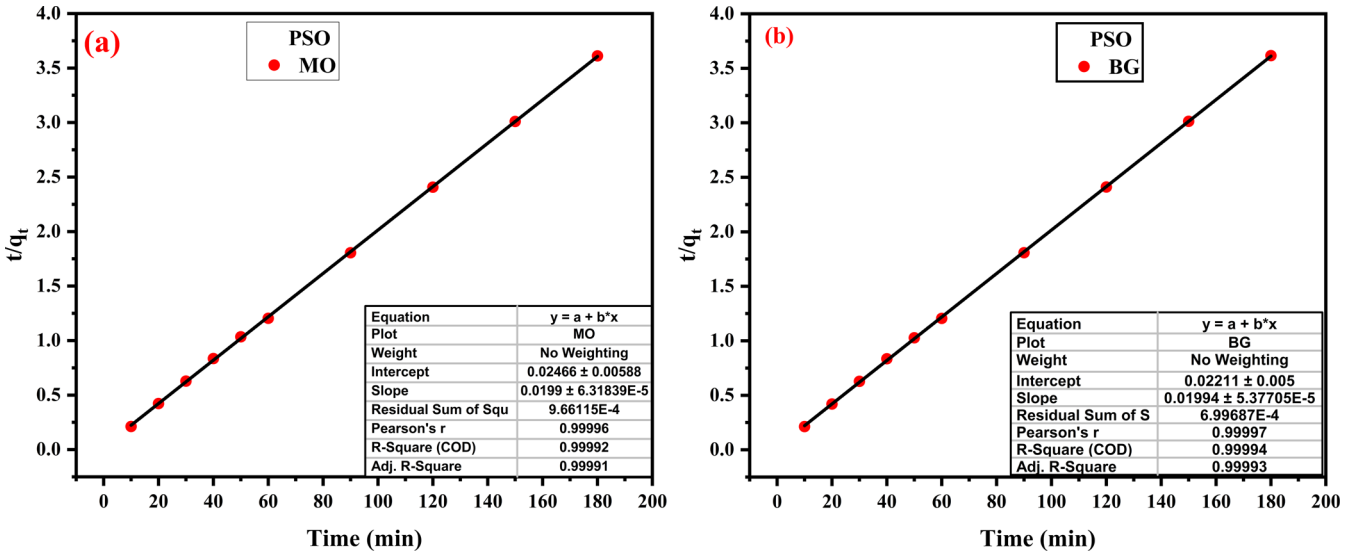

Figure 7. Pseudo-second-order kinetic model for the adsorption of MO (a) and BG (b) dyes.

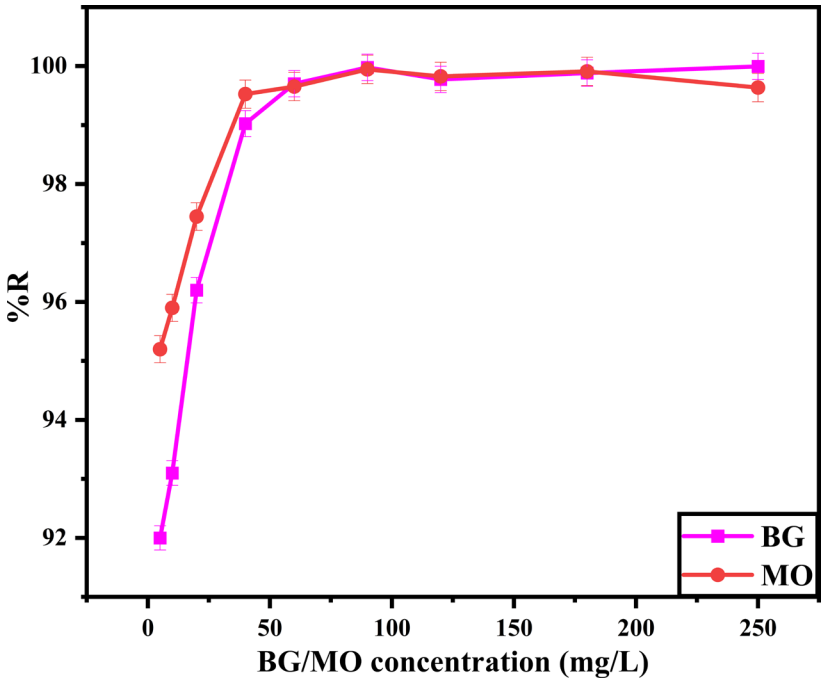

Figure 8. Effect of the initial MO and BG concentration on the NZC-*g*-PANI nanocomposite.

(b) Adsorption energy is the same for each ion and is independent of the covered surface.

The linear form of the pseudo-second-order kinetic model is as follows

$$\frac{t}{q_t} = \frac{1}{k_2 q_{e2}} + \frac{1}{q_t} \quad (4)$$

where K_2 is the rate constant for pseudo-second-order kinetics (g mg^{-1} min^{-1}).

Pseudo-second-order rate constant K_2, q_e, and correlation coefficient (R^2) were calculated from the slope and intercept of the plot (Figure 7a,b). R^2 for both dyes in Table 1 gave a value of 0.999, showing excellent linearity, which suggests that the adsorption of MO and BG can be illustrated by the PSO kinetic model.[37]

3.5. Dye Initial Concentration and Adsorption Isotherms. The initial adsorbate concentration is an important function that controls the process of adsorption. The effect of the initial adsorbate concentration was determined by preparing varying concentrations of MO and BG dyes (10−250) mg L^{-1} and then comparing them with %*R* (Figure 8) and adsorption capacity (Figure S6), keeping all other parameters (pH, adsorbent dose, and time) at optimum values. It is evidently clear from Figure 8 that the initial adsorption of BG and MO dyes increases up to 50 mg L^{-1} with an increase in initial dye concentration. On a further increase in dye concentration, no more dye adsorption takes place. Adsorption takes place in two phases: (a) at low concentrations, active sites present on the NZC-*g*-PANI adsorbent get occupied by BG and MO dyes by the adsorption process. (b) As the concentration of the targeted dye increases, the number

https://doi.org/10.1021/acsomega.2c04936
ACS Omega 2022, 7, 44836−44850

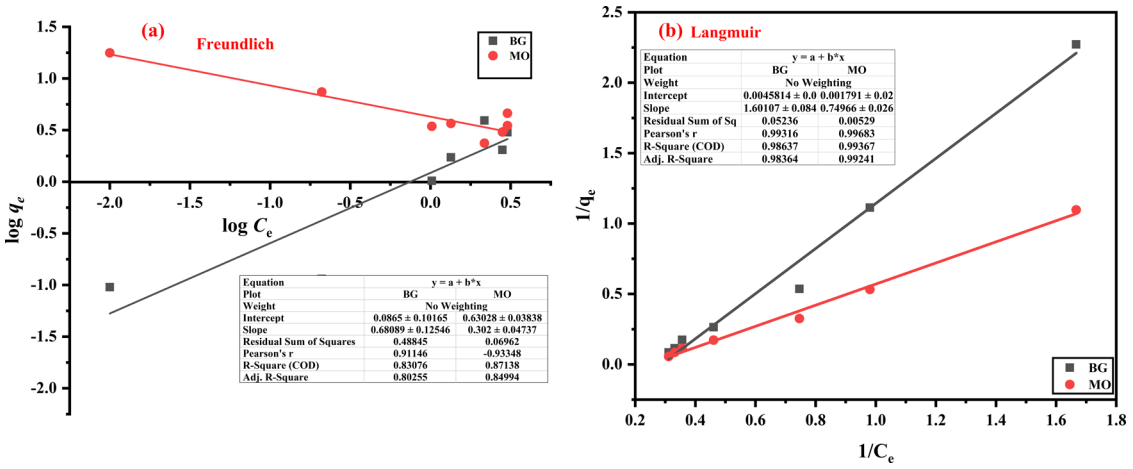

Figure 9. Freundlich (a) and Langmuir (b) isotherm plots for the adsorption of MO and BG dyes on NZC-*g*-PANI.

Table 2. Variables of Freundlich and Langmuir Models for the Adsorption of MO and BG Dyes on the NZC-*g*-PANI

	Langmuir model				Freundlich model		
dye	q^{max}(mg g^{-1})	K_l(L mg^{-1})	R_l	R^2	$1/n$	K_f(mg g^{-1})(L mg^{-1})$^{1/n}$	R^2
MO	558.34	0.0023	0.893	0.992	1.468	4.26	0.871
BG	218.27	0.0028	0.874	0.983	3.311	1.22	0.830

of finite active sites on the NZC-*g*-PANI adsorbent decreases, thus slowing the process of adsorption.

Adsorption isotherm implies that the amount of solute can be adsorbed onto an adsorbent, resulting in an equilibrium concentration of solute in the solution at a constant temperature. Accumulation of any substance over a solid surface is possible due to the interaction or attraction of the adsorbate over the adsorbent. These interactions are generally because of electrostatic forces referred to as van der Waals forces (VWFs). Many isotherm equations have been used to study the solute adsorbed by an adsorbent (per unit mass). In the current study, the most accepted adsorption models, Freundlich and Langmuir adsorption isotherms, have been used.

3.5.1. Freundlich Isotherm. The Freundlich isotherm is the earliest equation describing the adsorption process. The Freundlich adsorption isotherm shows the adsorption of an adsorbate on a heterogeneous surface, which is not confined to monolayer formation and shows various interactions that occur between adsorbed molecules.[18] For many systems, adsorption heat decreases with the adsorption rate. This has been explained by the Freundlich isotherm, which was proposed as an empirical isotherm and is explained by the linear equation, which can be used to calculate the constant of K_f and n.[2]

$$\log q_{eq} = \log K_f + 1/n \log C_{eq} \quad (5)$$

where q_{eq} (mg g^{-1}) is the amount of the solute adsorbed/unit weight of the adsorbent, C_{eq} (mg L^{-1}) is the equilibrium constant of the solute, K_f is the Freundlich constant, and $1/n$ is the adsorption intensity.

The graph between ln q_{eq} vs ln C_{eq} is shown in Figure 9a. R^2 values obtained from Table 2 for MO and BG are 0.871 and 0.830, respectively, which shows that the adsorption of both dyes does not follow this model.

3.5.2. Langmuir Isotherm. The Langmuir adsorption isotherm is used to explain the dynamic equilibrium stage between the adsorbate and the adsorbent, where the adsorption of the adsorbate is restricted to a single molecular layer or before a relative pressure of unity is obtained.

The Langmuir isotherm, which was proposed by Langmuir,[61] was considered suitable for describing the chemisorption process with the formation of covalent bonds between the adsorbate and the adsorbent, but the isotherm can be used to describe the binary adsorption behavior. The linear form of the Langmuir equation is represented by eq 6.

$$C_e/q_e = 1/Q_o b + 1/Q_o C_e \quad (6)$$

where C_e (mg L^{-1}) is the equilibrium concentration of the adsorbate in the aqueous phase. q_e (mg L^{-1}) is the equilibrium concentration of the adsorbate in the adsorbent phase. Q_o (mg g^{-1}) is the single-layer adsorption capacity, $b = K_a/K_b$, where K_a and K_b are the rate constants for the adsorption and desorption processes, respectively.

A graph of $1/q_e$ vs $1/C_e$ is shown in Figure 9b. Values of R^2 in Table 2 for the adsorption of MO and BG dyes are calculated as 0.992 and 0.983, respectively. It specifies the high potential of the Langmuir model for the adsorption of both BG and MO dyes. The Langmuir adsorption isotherm is the most commonly used model for pollutant adsorption from an aqueous solution, especially when adsorption takes place onto the adsorbent at specific sites. Table 2 and Figure 9b suggest that the removal of MO and BG is obtained on the heterogeneous surface of the NZC-*g*-PANI composite, and the formation of monolayer adsorption consequently supports the proposed chemisorption mechanism. The Langmuir maximum adsorption capacities of MO and BG dyes onto the NZC-*g*-PANI composite were up to 558.34 and 218.27 mg g^{-1}, respectively. Such high maximum adsorption capacities toward BG and MO may be attributed to multifunctional groups present on the surface of the NZC-*g*-PANI biosorbent. The adsorption capacity of as-prepared NZC-*g*-PANI for MO and BG dyes from aqueous solution is compared to another adsorbent, as given in Table S2.

https://doi.org/10.1021/acsomega.2c04936
ACS Omega 2022, 7, 44836−44850

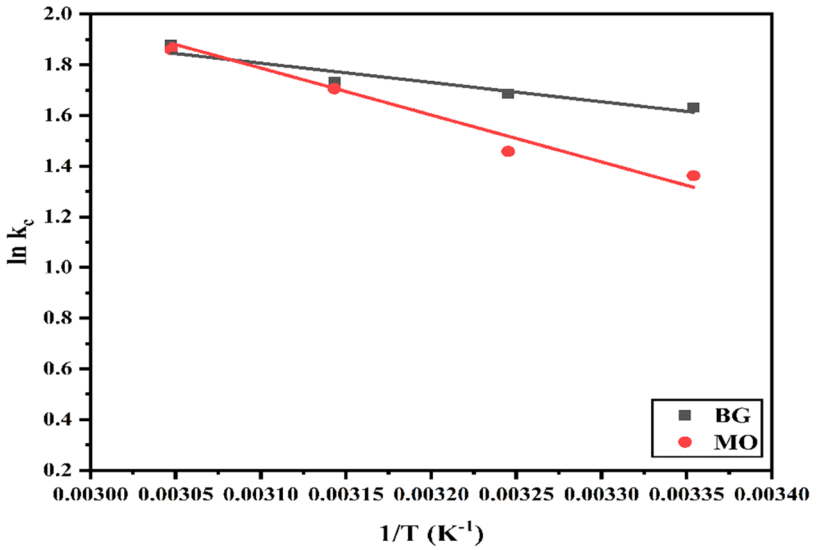

Figure 10. Graph between ln K_c and $1/T$ for BG and MO to show thermodynamic variables.

Table 3. Thermodynamic Variables for the Adsorption of MO and BG Dyes on the NZC-*g*-PANI

	K_c				$\Delta G°$ (kJ mol^{-1})					
dye	298.15 K	308.15 K	318.15 K	328.15 K	298.15 K	308.15 K	318.15 K	328.15 K	$\Delta H°$ (kJ mol^{-1})	$\Delta S°$ (J mol^{-1} K^{-1})
MO	23.06	25.04	63.93	72.31	−9.29	−9.94	−10.52	−11.15	6.32	34.61
BG	42.85	48.5	53.94	59.97	−7.75	−8.24	−10.97	−11.67	15.40	62.59

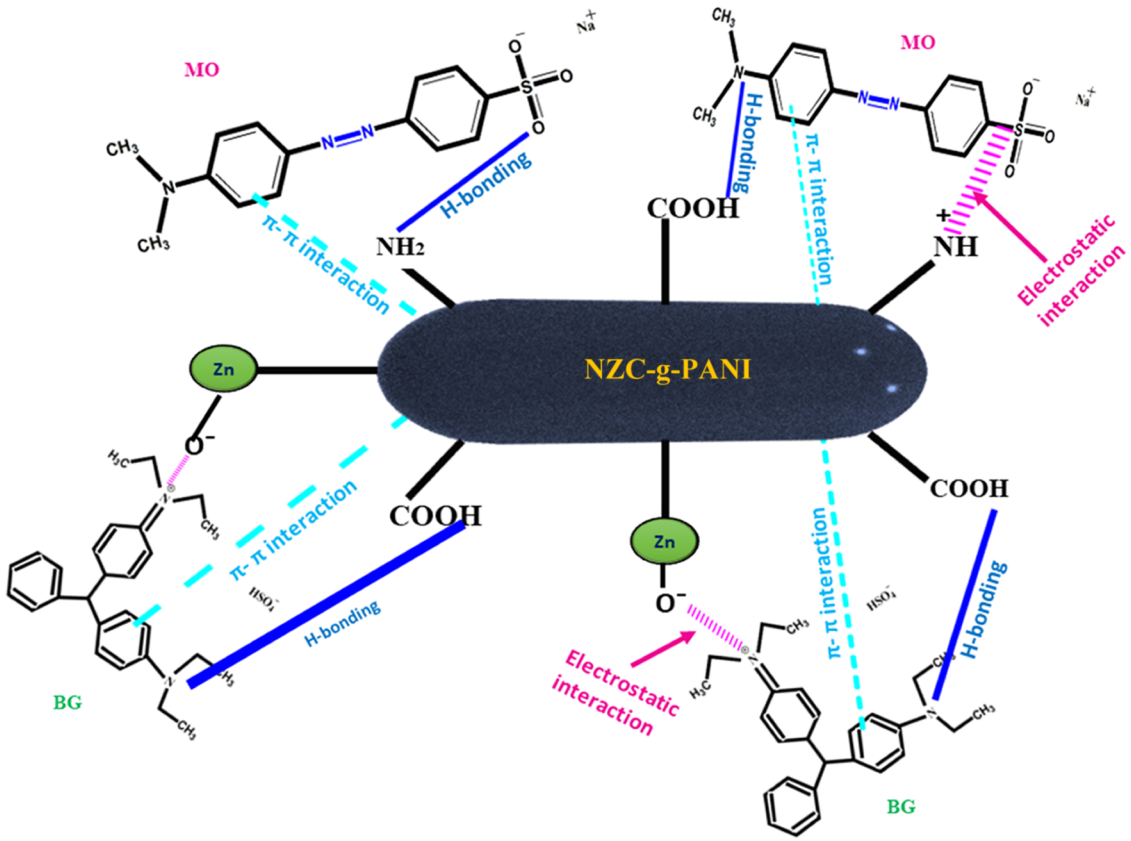

Figure 11. Proposed mechanism for the adsorption of BG and MO onto NZC-*g*-PANI.

3.6. Thermodynamic Study. Figure S7 shows the effect of temperature on the adsorption capacity of the NZC-*g*-PANI nanocomposite. The q_e of the NZC-*g*-PANI significantly increased with increasing temperature in the range of 298.15−328.15 K, which reached up to 199.5 mg g^{-1} for BG and 236 mg g^{-1} for MO dye at 323 K. The results suggest that

https://doi.org/10.1021/acsomega.2c04936
ACS Omega 2022, 7, 44836−44850

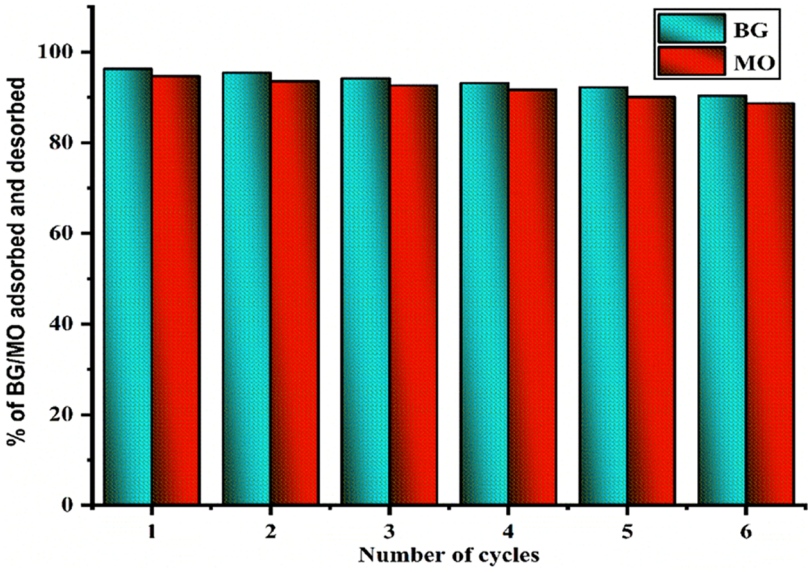

Figure 12. Recyclability test of the NZC-*g*-PANI nanocomposite for BG and MO dye removal.

targeted BG and MO adsorption on NZC-*g*-PANI is aided at higher temperatures. This result can be explained by the fact that the mobility and diffusion of BG and MO moieties enhance on increasing the temperature, causing an increase in contact with active adsorption sites on NZC-*g*-PANI.

Gibbs free energy (ΔG), enthalpy (ΔH), and entropy (ΔS), which are the various thermodynamic variables, were compared with the adsorption of MO and BG dyes onto the NZC-*g*-PANI nanocomposite. These were calculated using Gibbs free energy and the van't Hoff equation as follows

$$\Delta G = \Delta H - T\Delta S \tag{7}$$

$$\ln K_c = \Delta S/R - \Delta H/RT \tag{8}$$

where T denotes temperature in Kelvin, K_c represents the distribution coefficient of adsorption, and R is the universal gas constant.

A linear graph (Figure 10) was plotted between ln K_c and $1/T$ for MO and BG dyes to show the thermodynamic variables as given in Table 3. Negative values for BG and MO dyes can be seen for Gibbs free energy, and an increase in Gibbs free energy (ΔG) was witnessed with increasing temperature. The enthalpy change (ΔH) is positive for both MO and BG dyes, showing the endothermic nature of adsorption. Entropy (ΔS) is positive for both MO and BG dyes, showing an increase in randomness during the adsorption process.

3.7. Mechanism of BG and MO Biosorption onto NZC-*g*-PANI. It is very complex to understand the process of dye adsorption on the surface of the biosorbent because multiple types of factors participate in it between the adsorbate and the adsorbent. The interface and affinity of dye molecules with the adsorbent surface are influenced by the surface characteristics of the adsorbent, as well as the functional groups and molecular structure of the dyes.[18]

In this study, the proposed dye adsorption mechanism (Figure 11) is illustrated by FTIR spectra (Figure S8) the and SEM study (Figure 4) of the NZC-*g*-PANI nanocomposite before and after MO and BG adsorption. Before adsorption, the NZC-*g*-PANI IR peak has already been clarified in Section 3.1.1.

After BG dye adsorption onto the NZC-*g*-PANI biosorbent, FTIR spectra show a shift in band intensity from 3433 to 3431 cm^{-1} due to the hydrogen bond interaction between the polar N^+ atom of BG dye molecules and the NZC-*g*-PANI surface.[62,63] After BG dye adsorption, new peaks arise at 2337 cm^{-1}, which is attributed to the C═N stretching of the aromatic tertiary amine, and 637 cm^{-1}, which is attributed to the C−H stretching of benzene rings.[64] Furthermore, it is evident that the peak at 1581 cm^{-1} is allocated to the stretch vibration of the C═N bond of the quinoid structure of the BG dye.[65] After BG biosorption, it shifts to higher wavenumbers (1590 cm^{-1}), which discloses the participation of the quinoid structure in the adsorption process. The peak at 1215 cm^{-1}, which is attributed to the C−O stretching of the carboxylic group[66] on the surface of NZC-*g*-PANI, disappears after both BG and MO biosorption. It clearly indicates that carboxylic groups on the surface of NZC-*g*-PANI take part in both MO and BG dye removal via hydrogen bond formation. In the FTIR spectrum of MO-sorbed NZC-*g*-PANI (Figure S8) and BG-sorbed NZC-*g*-PANI (Figure S8), the vibrational band due to the aromatic C═C bond of the NZC-*g*-PANI bionanocomposite shifted in the range of 1620−1700 cm^{-1} to a higher wavelength. It is due to localization of aromatic π-electrons of NZC-*g*-PANI owing to the $\pi-\pi$ interactions of aromatic rings of both MO and BG dyes and NZC-*g*-PANI molecules.[67]

The value of pH_{pzc} of the NZC-*g*-PANI nanocomposite was recorded at 2.0 (Figure 5a). If pH is above 2.0, the surface of the NZC-*g*-PANI nanocomposite becomes negatively charged due to the presence of a hydroxyl (OH^-) group. Thus, the negatively charged surface of NZC-*g*-PANI interacts electrostatically with the N^+ atoms of BG molecules available in aqueous solution. Previous studies also show that electrostatic interaction strengthens the bond very strongly between the cationic dye and the adsorbent,[68] while, at pH < pH_{pzc}, the negatively charged sulfonic acid group ($-SO_3^-$) of the MO dye electrostatically interacted with the positively charged protonated PANI chain of the NZC-*g*-PANI biosorbent.[36] Furthermore, the adsorption of dye molecules on an adsorbent can also be governed by $\pi-\pi$ interaction. The NZC-*g*-PANI bionanocomposite has a C═C bond π-system due to the organic aromatic structure in PANI, which interacts with the π-

https://doi.org/10.1021/acsomega.2c04936
ACS Omega 2022, 7, 44836−44850

electron of the aromatic ring of BG as well as MO dyes via $\pi-\pi$ interaction. The $\pi-\pi$ interaction between the BG and MO dyes with the NZC-*g*-PANI biosorbent is supposed to be weaker than the electrostatic interaction.[64] The carboxyl (−COOH) group and water molecules on the surface of the NZC-*g*-PANI adsorbent offered H atoms to form hydrogen bonding (H-bonding) with the polar N^+ atoms of the BG dye. The hydroxyl group of NZC-*g*-PANI is also attached to the azo group of the MO dye by hydrogen bonding (Figure 11).[3] Overall, electrostatic interaction, $\pi-\pi$ bond interaction, and H-bonding are responsible for the biosorption of MO and BG dyes onto the NZC-*g*-PANI biosorbent.

3.8. Regeneration Study. In Figure 12, six regeneration adsorption capacities of NZC-*g*-PANI have been shown for both dyes. In the first cycle of BG and MO dyes, it was observed that the uptake abilities of NZC-*g*-PANI were 96.3 and 94.7%, respectively. In the subsequent cycles, the adsorption efficiency of NZC-*g*-PANI was slightly reduced for both dyes and reached 92.2 and 90.1% in the 5th cycle, respectively. However, in the 6th cycle, the uptake ability of NZC-*g*-PANI was further reduced, and equilibrium adsorption efficiencies of 90.4 and 88.7% were observed for BG and MO, respectively. This might be explained by the fact that the regeneration process may result in the diminution of binding sites on NZC-*g*-PANI, leaving some BG/MO dye moieties in the regenerated NZC-*g*-PANI biosorbent.[69] Consequently, the decrease in the uptake capacity of NZC-*g*-PANI is considerable, manifesting excellent reusability and outstanding regeneration behavior.

3.9. Application of NZC-*g*-PANI toward Real Water Samples. The practical application of the NZC-*g*-PANI biosorbent was also studied for real environmental samples from tap water (Faculty of Engineering and Technology, Jamia Millia Islamia, New Delhi, India), river water (Yamuna, New Delhi, India), and laundry wastewater (New Delhi, India). All samples were mixed individually with various concentrations of BG (10, 30, 50, and 100 mg L^{-1}) and MO (20, 40, 80, and 100 mg L^{-1}) dyes under optimum conditions. After treatment with the NZC-*g*-PANI biosorbent, the aliquots of the dyes were taken out from the reaction beaker, and unknown concentrations of the dyes were measured via ultraviolet−visible (UV−vis) spectrophotometry. The outcomes of real water samples presented in Table 4 show good removal efficiency (% *R*), which supports the validity of the proposed biosorbent, i.e., NZC-*g*-PANI, for the removal of targeted dyes from real samples.

4. CONCLUSIONS

In the current study, a multifunctionalized NZC-*g*-PANI bionanocomposite was prepared by the in situ polymerization method. The synthesized nanocomposite was characterized using FESEM, TEM, FTIR, Raman, and XRD analysis and was used as a novel adsorbent for the removal of MO and BG dyes from aqueous solution. The adsorption capacity was investigated as a function of pH, initial BG/MO adsorbate concentration, contact time, and NZC-*g*-PANI adsorbent dose. Based on the coefficient correlation (R^2) values of 0.992 and 0.983 for MO and BG, respectively, the Langmuir isotherm showed a better fit. Maximum adsorption capacities of 558.34 and 218.27 mg g^{-1} were obtained for MO and BG, respectively. Kinetic analysis revealed that the PSO model executed better than the PFO model. Thermodynamic studies revealed the endothermic and spontaneous nature of adsorption The magnitude of the enthalpy (ΔH) change was 6.32 and 15.40 kJ mol^{-1} for MO and BG, respectively, while entropy (ΔS) change values were 34.61 and 62.59 kJ mol^{-1} for MO and BG, respectively. The dye adsorption mechanism confirmed that $\pi-\pi$ interactions, electrostatic interactions, and hydrogen bonding are responsible to sequestrate both BG and MO dyes from aqueous solutions. The regeneration study showed that the NZC-*g*-PANI biosorbent had potential reusability for efficient BG and MO uptake up to six consecutive cycles. The efficacy of NZC-*g*-PANI on the real water sample presents excellent %*R* toward MO and BG dyes. From this study, it can be acknowledged that the synthesized bionanocomposite made up of NLP, ZnO, and L-cysteine-functionalized PANI can be used as a potential adsorbent for the removal of cationic and anionic dyes from synthetic as well as real water samples.

Table 4. Removal Efficiency of the NZC-*g*-PANI Nanocomposite for MO and BG Dyes from Tap Water, River Water, and Laundry Wastewater

real water sample	MO (mg L^{-1})	BG (mg L^{-1})	MO (% *R*)	BG (% *R*)
tap water	20	10	95.6	89.4
	40	30	92.7	81.3
	80	50	87.4	73.6
	100	100	78.7	64.6
river water	20	10	89.5	76.8
	40	30	80.9	67.8
	80	50	75.4	56.4
	100	100	65.9	43.9
laundry wastewater	20	10	94.2	85.3
	40	30	85.4	79.3
	80	50	75.6	67.3
	100	100	67.6	53.1

■ ASSOCIATED CONTENT

Supporting Information

The Supporting Information is available free of charge at https://pubs.acs.org/doi/10.1021/acsomega.2c04936.

Structure of various dyes used in the current study; dyes used in the current study, their features and ecotoxicological effects; removal efficiency of MO, BG, AB 10B, CV, EBT, and MB dyes on NZC-*g*-PANI at neutral pH; %*R* of pristine NLP, pristine ZnO, pristine PANI, and NZC-*g*-PANI for MO and BG dyes at neutral pH; Raman spectra of NLP; effect of contact time (a); pseudo-first-order kinetic model for the adsorption of MO and BG dyes (b) onto the NZC-*g*-PANI nanocomposite; adsorption capacity of NZC-*g*-PANI against BG (a) and MO (b) dyes; variation of the adsorption amount of BG (a) and MO (b) with increasing temperature for the NZC-*g*-PANI nanocomposite; and FTIR spectra of NZC-*g*-PANI (a), MO-sorbed NZC-*g*-PANI (b), and BG-sorbed NZC-*g*-PANI (c) (PDF)

■ AUTHOR INFORMATION

Corresponding Authors

Mohd Saquib Tanweer − *Environmental Science Research Lab, Department of Applied Sciences & Humanities, Faculty of Engineering & Technology, Jamia Millia Islamia, New Delhi 110025, India;* orcid.org/0000-0001-5401-0667; Email: saquibtanweer701@gmail.com

https://doi.org/10.1021/acsomega.2c04936
ACS Omega 2022, 7, 44836−44850

Masood Alam − *Environmental Science Research Lab, Department of Applied Sciences & Humanities, Faculty of Engineering & Technology, Jamia Millia Islamia, New Delhi 110025, India*; Email: malam@jmi.ac.in

Authors

Ritu Bir − *Department of Chemistry, Galgotias University, Noida 203201 Uttar Pradesh, India*

Meenakshi Singh − *Department of Chemistry, Galgotias University, Noida 203201 Uttar Pradesh, India*

Complete contact information is available at: https://pubs.acs.org/10.1021/acsomega.2c04936

Author Contributions

§R.B. and M.S.T. are equal authors.

Notes

The authors declare no competing financial interest.

■ ACKNOWLEDGMENTS

One of the authors, M.S.T., is thankful to the University Grants Commission (UGC) for the Non-NET Fellowship.

■ REFERENCES

(1) Tripathy, B. K.; Kumar, S.; Kumar, M.; Debnath, A. Microwave Induced Catalytic Treatment of Brilliant Green Dye with Carbon Doped Zinc Oxide Nanoparticles: Central Composite Design, Toxicity Assessment and Cost Analysis. *Environ. Nanotechnol., Monit. Manage.* **2020**, *14*, No. 100361.

(2) Ahmad, R.; Ansari, K. Chemically Treated *Lawsonia inermis* Seeds Powder (CTLISP): An Eco-Friendly Adsorbent for the Removal of Brilliant Green Dye from Aqueous Solution. *Groundwater Sustainable Dev.* **2020**, *11*, No. 100417.

(3) Ahmad, R.; Kumar, R. Conducting Polyaniline/Iron Oxide Composite: A Novel Adsorbent for the Removal of Amido Black 10B. *J. Chem. Eng. Data* **2010**, *55*, 3489−3493.

(4) Iqbal, Z.; Tanweer, M. S.; Alam, M. Recent Advances in Adsorptive Removal of Wastewater Pollutants by Chemically Modified Metal Oxides: A Review. *J. Water Process Eng.* **2022**, *46*, No. 102641.

(5) Dutta, S.; Srivastava, S. K.; Gupta, B.; Gupta, A. K. Hollow Polyaniline Microsphere/MnO2/Fe3O4nanocomposites in Adsorptive Removal of Toxic Dyes from Contaminated Water. *ACS Appl. Mater. Interfaces* **2021**, *13*, 54324−54338.

(6) Kishor, R.; Purchase, D.; Saratale, G. D.; Romanholo Ferreira, L. F.; Hussain, C. M.; Mulla, S. I.; Bharagava, R. N. Degradation Mechanism and Toxicity Reduction of Methyl Orange Dye by a Newly Isolated Bacterium *Pseudomonas aeruginosa* MZ520730. *J. Water Process Eng.* **2021**, *43*, No. 102300.

(7) Tanweer, M. S.; Iqbal, Z.; Alam, M. Experimental Insights into Mesoporous Polyaniline-Based Nanocomposites for Anionic and Cationic Dye Removal. *Langmuir* **2022**, *38*, 8837−8853.

(8) Peydayesh, M.; Suta, T.; Usuelli, M.; Handschin, S.; Canelli, G.; Bagnani, M.; Mezzenga, R. Sustainable Removal of Microplastics and Natural Organic Matter from Water by Coagulation-Flocculation with Protein Amyloid Fibrils. *Environ. Sci. Technol.* **2021**, *55*, 8848−8858.

(9) Dominguez-Ramos, A.; Chavan, K.; García, V.; Jimeno, G.; Albo, J.; Marathe, K. V.; Yadav, G. D.; Irabien, A. Arsenic Removal from Natural Waters by Adsorption or Ion Exchange: An Environmental Sustainability Assessment. *Ind. Eng. Chem. Res.* **2014**, *53*, 18920−18927.

(10) Malaeb, L.; Ayoub, G. M. Reverse Osmosis Technology for Water Treatment: State of the Art Review. *Desalination* **2011**, *267*, 1−8.

(11) Ahmad, S.; Siddiqi, W. A.; et al. Facile Hydrophilic Chitosan and Graphene Oxide Modified Sustainable Non-Woven Fabric Composite Sieve Membranes (NWF@Cs/Gx): Antifouling, Protein Rejection, and Oil-Water Emulsion Separation Studies. *Chem. Eng. Res. Des.* **2022**, *181*, 220−238.

(12) Zolezzi, C.; Ihle, C. F.; Angulo, C.; Palma, P.; Palza, H. Effect of the Oxidation Degree of Graphene Oxides on Their Adsorption, Flocculation, and Antibacterial Behavior. *Ind. Eng. Chem. Res.* **2018**, *57*, 15722−15730.

(13) Tanweer, M. S.; Alam, M.Novel 2D Nanomaterial Composites Photocatalysts: Application in Degradation of Water Contaminants. In *2D Nanomaterials for Energy and Environmental Sustainability*; Springer: Singapore, 2022; pp 75−96.

(14) Ahmad, S.; Siddiqui, V. U.; Ansari, A.; Siddiqi, W. A.; Akram, M. K. In *Effective Photocatalytic Activity of Graphene/Polyindole Nanocomposites to Degrade the Herbicide 2,4-Dichlorophenoxyacetic Acid (2,4-D) for Water Treatment*, AIP Conference Proceedings; AIP Publishing LLC, 2020; Vol. 2276, p 020016.

(15) Danish, M.; Muneer, M. Facile Synthesis of Highly Efficient Co@ZnSQDs/g-C3N4/MWCNT Nanocomposites and Their Photocatalytic Potential for the Degradation of RhB Dye: Efficiency, Degradation Kinetics, and Mechanism Pathway. *Ceram. Int.* **2021**, *47*, 13043−13056.

(16) Ahmad, R.; Ansari, K. Comparative Study for Adsorption of Congo Red and Methylene Blue Dye on Chitosan Modified Hybrid Nanocomposite. *Process Biochem.* **2021**, *108*, 90−102.

(17) Tanweer, M. S.; Chauhan, H.; Alam, M.Advanced 2D Nanomaterial Composites: Applications in Adsorption of Water Pollutants and Toxic Gases. In *2D Nanomaterials for Energy and Environmental Sustainability*; Springer: Singapore, 2022; pp 97−124.

(18) Ahmad, R.; Ansari, K. Enhanced Sequestration of Methylene Blue and Crystal Violet Dye onto Green Synthesis of Pectin Modified Hybrid (Pect/AILP-Kal) Nanocomposite. *Process Biochem.* **2021**, *111*, 132−143.

(19) Zeng, S.; Long, J.; Sun, J.; Wang, G.; Zhou, L. A Review on Peach Gum Polysaccharide: Hydrolysis, Structure, Properties and Applications. *Carbohydr. Polym.* **2022**, *279*, No. 119015.

(20) Bhattacharyya, K. G.; Sharma, A. *Azadirachta indica* Leaf Powder as an Effective Biosorbent for Dyes: A Case Study with Aqueous Congo Red Solutions. *J. Environ. Manage.* **2004**, *71*, 217−229.

(21) Naghdi, M.; Taheran, M.; Brar, S. K.; Verma, M.; Surampalli, R. Y.; Valero, J. R. Green and Energy-Efficient Methods for the Production of Metallic Nanoparticles. *Beilstein J. Nanotechnol.* **2015**, *6*, 2354−2376.

(22) Mohan Kumar, K.; Mandal, B. K.; Siva Kumar, K.; Sreedhara Reddy, P.; Sreedhar, B. Biobased Green Method to Synthesise Palladium and Iron Nanoparticles Using *Terminalia chebula* Aqueous Extract. *Spectrochim. Acta, Part A* **2013**, *102*, 128−133.

(23) Das, R. K.; Pachapur, V. L.; Lonappan, L.; Naghdi, M.; Pulicharla, R.; Maiti, S.; Cledon, M.; Dalila, L. M. A.; Sarma, S. J.; Brar, S. K. Biological Synthesis of Metallic Nanoparticles: Plants, Animals and Microbial Aspects. *Nanotechnol. Environ. Eng.* **2017**, *2*, No. 18.

(24) Rashtbari, Y.; Afshin, S.; Hamzezadeh, A.; Abazari, M.; Poureshgh, Y.; Fazlzadeh, M. Application of Powdered Activated Carbon Coated with Zinc Oxide Nanoparticles Prepared Using a Green Synthesis in Removal of Reactive Blue 19 and Reactive Black-5: Adsorption Isotherm and Kinetic Models. *Desalin. Water Treat.* **2020**, *179*, 354−367.

(25) Zhang, Y.; Yang, Z.; Yu, Y.; Wen, B.; Liu, Y.; Qiu, M. Tunable Electromagnetic Interference Shielding Ability in a One-Dimensional Bagasse Fiber/Polyaniline Heterostructure. *ACS Appl. Polym. Mater.* **2019**, *1*, 737−745.

(26) Yun, J.; Echols, I.; Flouda, P.; Wang, S.; Easley, A.; Zhao, X.; Tan, Z.; Prehn, E.; Zi, G.; Radovic, M.; Green, M. J.; Lutkenhaus, J. L. Layer-by-Layer Assembly of Polyaniline Nanofibers and MXene Thin-Film Electrodes for Electrochemical Energy Storage. *ACS Appl. Mater. Interfaces* **2019**, *11*, 47929−47938.

(27) He, Z.; Xie, H.; Wu, H.; Chen, J.; Ma, S.; Duan, X.; Chen, A.; Kong, Z. Recent Advances in MXene/Polyaniline-Based Composites

for Electrochemical Devices and Electromagnetic Interference Shielding Applications. *ACS Omega* **2021**, *6*, 22468−22477.
(28) Nasar, A.; Mashkoor, F. Application of Polyaniline-Based Adsorbents for Dye Removal from Water and Wastewater—a Review. *Environ. Sci. Pollut. Res.* **2019**, *26*, 5333−5356.
(29) Parangusan, H.; Bhadra, J.; Ahmad, Z.; Mallick, S.; Touati, F.; Al-Thani, N. Humidity Sensor Based on Poly(Lactic Acid)/PANI−ZnO Composite Electrospun Fibers. *RSC Adv.* **2021**, *11*, 28735−28743.
(30) Ali, S.; Tanweer, M. S.; Alam, M. Kinetic, Isothermal, Thermodynamic and Adsorption Studies on *Mentha piperita* Using ICP-OES. *Surf. Interfaces* **2020**, *19*, No. 100516.
(31) Ahmad, R.; Ansari, K. Novel In-Situ Fabrication of L-Methionine Functionalized Bionanocomposite for Adsorption of Amido Black 10B Dye. *Process Biochem.* **2022**, *119*, 48−57.
(32) Singh, K.; Bharose, R.; Verma, S. K.; Singh, V. K. Potential of Powdered Activated Mustard Cake for Decolorising Raw Sugar. *J. Sci. Food Agric.* **2013**, *93*, 157−165.
(33) Anand, A.; Rani, N.; Saxena, P.; Bhandari, H.; Dhawan, S. K. Development of Polyaniline/Zinc Oxide Nanocomposite Impregnated Fabric as an Electrostatic Charge Dissipative Material. *Polym. Int.* **2015**, *64*, 1096−1103.
(34) Muhammad, W.; Ullah, N.; Haroon, M.; Abbasi, B. H. Optical, Morphological and Biological Analysis of Zinc Oxide Nanoparticles (ZnO NPs) Using *Papaver somniferum* L. *RSC Adv.* **2019**, *9*, 29541−29548.
(35) Anand, A.; Rani, N.; Saxena, P.; Bhandari, H.; Dhawan, S. K. Development of Polyaniline/Zinc Oxide Nanocomposite Impregnated Fabric as an Electrostatic Charge Dissipative Material. *Polym. Int.* **2015**, *64*, 1096−1103.
(36) Jahan, K.; Tyeb, S.; Kumar, N.; Verma, V. Bacterial Cellulose-Polyaniline Porous Mat for Removal of Methyl Orange and Bacterial Pathogens from Potable Water. *J. Polym. Environ.* **2021**, *29*, 1257−1270.
(37) Razzaq, S.; Akhtar, M.; Zulfiqar, S.; Zafar, S.; Shakir, I.; Agboola, P. O.; Haider, S.; Warsi, M. F. Adsorption Removal of Congo Red onto L-Cysteine/RGO/PANI Nanocomposite: Equilibrium, Kinetics and Thermodynamic Studies. *J. Taibah Univ. Sci.* **2021**, *15*, 50−62.
(38) Yslas, E. I.; Cavallo, P.; Acevedo, D. F.; Barbero, C. A.; Rivarola, V. A. Cysteine Modified Polyaniline Films Improve Biocompatibility for Two Cell Lines. *Mater. Sci. Eng. C* **2015**, *51*, 51−56.
(39) Ibrahim, K. A. Synthesis and Characterization of Polyaniline and Poly(Aniline-Co-o-Nitroaniline) Using Vibrational Spectroscopy. *Arab. J. Chem.* **2017**, *10*, S2668−S2674.
(40) Spectroscopic Study of Polyaniline Emeraldine Base: Modelling Approach | Semantic Scholar. https://www.semanticscholar.org/paper/Spectroscopic-Study-of-Polyaniline-Emeraldine-Base%3A-Ibrahim-Koglin/ade2955a289db29d978c73c7d5f85055077f3fab (accessed May 22, 2022).
(41) Ratsameetammajak, N.; Thanapat, A.; Torranin, C.; Hiroki, K.; Ai-shui, Yu.; Thapanee, S. Rice Husk-Derived Nano-SiO_2 Assembled on Reduced Graphene Oxide Distributed on Conductive Flexible Polyaniline Frameworks towards High-Performance Lithium-Ion Batteries. *RSC Adv.* **2022**, *12*, 14621−14630.
(42) Alam, M.; Rais, S.; Aslam, M. Role of *Azadirachta indica* (Neem) Biomass in the Removal of Ni(II) from Aqueous Solution. *Desalin. Water Treat.* **2010**, *21*, 220−227.
(43) Das, R.; Mukherjee, A.; Sinha, I.; Roy, K.; Dutta, B. K. Synthesis of Potential Bio-Adsorbent from Indian Neem Leaves (*Azadirachta indica*) and Its Optimization for Malachite Green Dye Removal from Industrial Wastes Using Response Surface Methodology: Kinetics, Isotherms and Thermodynamic Studies. *Appl. Water Sci.* **2020**, *10*, No. 117.
(44) Maruthupandy, M.; Qin, P.; Muneeswaran, T.; Rajivgandhi, G.; Quero, F.; Song, J. M. Graphene-Zinc Oxide Nanocomposites (G-ZnO NCs): Synthesis, Characterization and Their Photocatalytic Degradation of Dye Molecules. *Mater. Sci. Eng. B* **2020**, *254*, No. 114516.
(45) Chen, Y. L.; Hu, Z. A.; Chang, Y. Q.; Wang, H. W.; Zhang, Z. Y.; Yang, Y. Y.; Wu, H. Y. Zinc Oxide/Reduced Graphene Oxide Composites and Electrochemical Capacitance Enhanced by Homogeneous Incorporation of Reduced Graphene Oxide Sheets in Zinc Oxide Matrix. *J. Phys. Chem. C* **2011**, *115*, 2563−2571.
(46) Patil, P. T.; Anwane, R. S.; Kondawar, S. B. Development of Electrospun Polyaniline/ZnO Composite Nanofibers for LPG Sensing. *Procedia Mater. Sci.* **2015**, *10*, 195−204.
(47) Šćepanović, M.; Grujić-Brojčin, M.; Vojisavljević, K.; Bernikc, S.; Srećković, T. Raman Study of Structural Disorder in ZnO Nanopowders. *J. Raman Spectrosc.* **2010**, *41*, 914−921.
(48) Zeise, I.; Heiner, Z.; Holz, S.; Joester, M.; Büttner, C.; Kneipp, J. Raman Imaging of Plant Cell Walls in Sections of *Cucumis sativus*. *Plants* **2018**, *7*, No. 7.
(49) Yin, C.; Gao, L.; Zhou, F.; Duan, G. Facile Synthesis of Polyaniline Nanotubes Using Self-Assembly Method Based on the Hydrogen Bonding: Mechanism and Application in Gas Sensing. *Polymers* **2017**, *9*, No. 544.
(50) Ramalingam, R.··· H. A.-L.-D. J.. Synthesis, surface and textural characterization of Ag doped polyaniline-SiO2(Pan-Ag/RHA) Nanocomposites derived from chalcogen.ro. 2016; *113*, 731−740.
(51) Ben Ali, M.; Wang, F.; Boukherroub, R.; Lei, W.; Xia, M. Phytic Acid-Doped Polyaniline Nanofibers-Clay Mineral for Efficient Adsorption of Copper (II) Ions. *J. Colloid Interface Sci.* **2019**, *553*, 688−698.
(52) Huang, K.; Zhang, Y.; Long, Y.; Yuan, J.; Han, D.; Wang, Z.; Niu, L.; Chen, Z. Preparation of Highly Conductive, Self-Assembled Gold/Polyaniline Nanocables and Polyaniline Nanotubes. *Chem. − Eur. J.* **2006**, *12*, 5314−5319.
(53) Zujovic, Z. D.; Laslau, C.; Bowmaker, G. A.; Kilmartin, P. A.; Webber, A. L.; Brown, S. P.; Travas-Sejdic, J. Role of Aniline Oligomeric Nanosheets in the Formation of Polyaniline Nanotubes. *Macromolecules* **2010**, *43*, 662−670.
(54) Ran, F.; Tan, Y. T.; Liu, J.; Zhao, L.; Kong, L. B.; Luo, Y. C.; Kang, L. Preparation of Hierarchical Polyaniline Nanotubes Based on Self-Assembly and Its Electrochemical Capacitance. *Polym. Adv. Technol.* **2012**, *23*, 1297−1301.
(55) El-Azazy, M.; Dimassi, S. N.; El-Shafie, A. S.; Issa, A. A. Bio-Waste Aloe Vera Leaves as an Efficient Adsorbent for Titan Yellow from Wastewater: Structuring of a Novel Adsorbent Using Plackett-Burman Factorial Design. *Appl. Sci.* **2019**, *9*, No. 4856.
(56) Hsini, A.; Naciri, Y.; Laabd, M.; El Ouardi, M.; Ajmal, Z.; Lakhmiri, R.; Boukherroub, R.; Albourine, A. Synthesis and Characterization of Arginine-Doped Polyaniline/Walnut Shell Hybrid Composite with Superior Clean-up Ability for Chromium (VI) from Aqueous Media: Equilibrium, Reusability and Process Optimization. *J. Mol. Liq.* **2020**, *316*, No. 113832.
(57) Martins, L. R.; Rodrigues, J. A. V.; Adarme, O. F. H.; Melo, T. M. S.; Gurgel, L. V. A.; Gil, L. F. Optimization of Cellulose and Sugarcane Bagasse Oxidation: Application for Adsorptive Removal of Crystal Violet and Auramine-O from Aqueous Solution. *J. Colloid Interface Sci.* **2017**, *494*, 223−241.
(58) Eltaweil, A. S.; El-Tawil, A. M.; Abd El-Monaem, E. M.; El-Subruiti, G. M. Zero Valent Iron Nanoparticle-Loaded Nanobentonite Intercalated Carboxymethyl Chitosan for Efficient Removal of Both Anionic and Cationic Dyes. *ACS Omega* **2021**, *6*, 6348−6360.
(59) Singh, S.; Gupta, H.; Dhiman, S.; Sahu, N. K. Decontamination of Cationic Dye Brilliant Green from the Aqueous Media. *Appl. Water Sci.* **2022**, *12*, No. 61.
(60) Ho, Y. S.; McKay, G. Pseudo-Second Order Model for Sorption Processes. *Process Biochem.* **1999**, *34*, 451−465.
(61) Langmuir, I. The Adsorption of Gases on Plane Surfaces of Glass, Mica and Platinum. *J. Am. Chem. Soc.* **1918**, *40*, 1361−1403.
(62) Navale, S. T.; Mali, V. V.; Pawar, S. A.; Mane, R. S.; Naushad, M.; Stadler, F. J.; Patil, V. B. Electrochemical Supercapacitor Development Based on Electrodeposited Nickel Oxide Film. *RSC Adv.* **2015**, *5*, 51961−51965.
(63) Mansour, R. A. E. G.; Simeda, M. G.; Zaatout, A. A. Removal of Brilliant Green Dye from Synthetic Wastewater under Batch Mode

https://doi.org/10.1021/acsomega.2c04936
ACS Omega 2022, 7, 44836−44850

Using Chemically Activated Date Pit Carbon. *RSC Adv.* **2021**, *11*, 7851−7861.
(64) Kataria, N.; Garg, V. K. Application of EDTA Modified Fe3O4/Sawdust Carbon Nanocomposites to Ameliorate Methylene Blue and Brilliant Green Dye Laden Water. *Environ. Res.* **2019**, *172*, 43−54.
(65) Tavlieva, M. P.; Genieva, S. D.; Georgieva, V. G.; Vlaev, L. T. Kinetic Study of Brilliant Green Adsorption from Aqueous Solution onto White Rice Husk Ash. *J. Colloid Interface Sci.* **2013**, *409*, 112−122.
(66) Jassim, A. H. M.; Banimuslem, H. A. In *Characterization and Sensing Application of Modified Multi Walled Carbon Nanotubes/Metal Phthalocyanine Thin Films*, AIP Conference Proceedings; AIP Publishing LLC, 2020; Vol. 12290, p 050009.
(67) Pereira, M. F. R.; Soares, S. F.; Órfão, J. J. M.; Figueiredo, J. L. Adsorption of Dyes on Activated Carbons: Influence of Surface Chemical Groups. *Carbon* **2003**, *41*, 811−821.
(68) Saini, J.; Garg, V. K.; Gupta, R. K. Removal of Methylene Blue from Aqueous Solution by Fe3O4@Ag/SiO2 Nanospheres: Synthesis, Characterization and Adsorption Performance. *J. Mol. Liq.* **2018**, *250*, 413−422.
(69) Ali, M. A.; Mubarak, M. F.; Keshawy, M.; Zayed, M. A.; Ataalla, M. Adsorption of Tartrazine Anionic Dye by Novel Fixed Bed Core-Shell-Polystyrene Divinylbenzene/Magnetite Nanocomposite. *Alexandria Eng. J.* **2022**, *61*, 1335−1352.

https://doi.org/10.1021/acsomega.2c04936
ACS Omega 2022, 7, 44836−44850